Bond-order potential for simulations of extended defects in tungsten

M. Mrovec,[1,2,*] R. Gröger,[3] A. G. Bailey,[3] D. Nguyen-Manh,[4] C. Elsässer,[1,2] and V. Vitek[3]

[1] *IZBS, University of Karlsruhe, Kaiserstr. 12, 76131 Karlsruhe, Germany*
[2] *Fraunhofer-Institute for Mechanics of Materials IWM, Wöhlerstr. 11, 79108 Freiburg, Germany*
[3] *Department of Materials Science and Engineering, University of Pennsylvania, Philadelphia, Pennsylvania, 19104-6267, USA*
[4] *EURATOM/UKAEA Fusion Association, Culham Science Centre, Abingdon, OX14 3DB, United Kingdom*

(Dated: November 24, 2006)

This paper presents the bond-order potential (BOP) for the BCC transition metal tungsten, which is a real-space semi-empirical method for the description of interactions between atoms. It is based on the tight-binding approximation and provides thus a direct bridge between the electronic-structure and the atomistic modeling hierarchies. Two variants of the BOP were constructed and they are both extensively tested against accurate DFT methods in order to assess their reliability and applicability. A comparison of BOP with a central-force potential on the other hand highlights the importance of directional bonding and demonstrates that a correct description of directional covalent bonds is crucial for a successful, fully transferable model. The potentials are applied in studies of low-index surfaces, symmetrical tilt grain boundaries and dislocations.

PACS numbers: 71.15.Nc, 71.20.Be, 61.72.Bb, 62.25.+g

I. INTRODUCTION

Tungsten is a refractory transition metal with a half-filled d-band, crystallizing in a body-centered-cubic (BCC) structure. It is a metal with the highest melting temperature (3680 K) and for this reason its main applications have been filaments for bulb lamps, electrical contacts, arch-welding electrodes, heating elements in high temperature furnaces, etc. Notwithstanding, two recent developments may broaden significantly the use of tungsten and elevate its technological prominence. First, tungsten is considered as one of the structural materials that will play an important role in the fusion reactor ITER project.[1,2] It is a promising plasma facing material, for both the divertor and the first wall, principally because of its high melting temperature and resistance to sputtering by low energy ions.[3,4] Second, recent advancements in nanoengineering have enabled tailoring of microstructure and production of ultrafine-grained and nanocrystalline tungsten with significantly enhanced mechanical behavior.[5] This nanoengineered material displays very high strength but localized shearing rather than uniform plastic deformation and/or cracking under loading.

An important general drawback in structural applications is the fact that in tungsten the ductile-to-brittle transition (DBT) occurs well above the room temperature.[6,7] This transition appears to be controlled by dislocation mobility rather than by crack nucleation.[8–10] For example, studies of the cleavage in tungsten single crystals indicate an anisotropy with respect to both the crack plane and the direction of crack propagation,[11] suggesting that the DBT temperature and subsequent crack extension are directly related to atomic level features of crack and dislocation propagation. In addition, the mechanical properties of tungsten are strongly dependent on alloying, impurities and thermomechanical treatment[12], which is a common characteristic of BCC transition metals (see e.g. Refs. 13,14). This is particularly important for fusion reactors since under prolonged irradiation by 14 MeV neutrons a significant transmutation of tungsten to osmium via rhenium takes place. Concerns have been expressed regarding mechanical properties of resulting W-Os-Re alloys, in particular in connection with embrittlement and occurrence of the sigma phase.[15]

The plastic deformation and fracture of crystalline materials is, in general, controlled by extended defects, specifically dislocations, grain boundaries and other interfaces.[16–20] For example, it is now generally accepted that in BCC metals the strong temperature dependence of the yield and flow stress arises owing to the complex structure of the core of $1/2\langle 111\rangle$ screw dislocations. Moreover, this core structure is responsible for unusual dependencies of the flow stress on the orientation of the crystal with respect to the loading axes (for reviews see Refs. 14,21–27). In tungsten the temperature and strain rate dependencies were observed in Refs. 28,29. Atomic level understanding of dislocation cores and their effects on dislocation glide, phenomena associated with formation and propagation of cleavage and/or intergranular cracks as well as investigation of the structure and properties of nano-crystalline materials, are typical problems that are studied by the atomic level computer modeling. Such studies have become wide-spread in materials science, as demonstrated by a recent handbook that summarizes a broad range of methods and specific investigations.[30]

The principal precursor of all atomic level calculations, in particular those involving systems composed of a large number of atoms that do not form an ideal lattice, is a reliable description of interatomic interactions. The state-of-the-art methods based on the density functional theory (DFT) provide such a description most reliably

and have, indeed, been employed in many investigations of physical and mechanical properties of materials (for reviews see for example Refs. 30–33). However, in studies of crystal defects these rigorous calculations are still limited by feasible block sizes and by the use of periodic boundary conditions. The DFT calculations are therefore commonly performed for periodic arrays of defects that are often too closely spaced. Consequently, studies of large and complex systems require approximations and simplifications when describing interatomic interactions that may, however, obliterate some important features of the chemical bonding. For this reason, the most challenging aspect of materials modeling is an appropriate description of interactions that reflects correctly and with sufficient accuracy the physics of bonding, while at the same time it is computationally treatable for large systems of particles.[34]

Methods describing interatomic forces that have been most broadly used in large-scale atomistic studies of metallic materials are the embedded atom method[35–37] and the Finnis-Sinclair (FS) potential.[34,38,39] These central-force many-body potentials are able to describe well simple and noble metals in which the bonding is almost nearly free-electron-like (NFE). However, in transition metals and intermetallic compounds based on transition metals, the bonding has a mixed NFE and covalent character. In these materials it is the filling of the d-band that controls the cohesion and hence the particular ground state structure.[40,41] This bonding, which is mediated by the d-electrons, is covalent in character so that the atomic interactions are non-central and depend on the angles between bonds.

Various approximate schemes that include non-central forces in metallic materials have been advanced in the recent years. They range from the modified embedded atom method[42–44] through a variety of tight-binding (TB) techniques (see e.g. Ref. 45) to the approach based on perturbation expansions employed in the framework of first-principles generalized pseudopotential theory.[46,47] The development we focus on in this paper is the Bond-Order Potential (BOP). This method possesses an important advantage for modeling of extended defects since it can be utilized in real space and periodic boundary conditions, necessary in k-space methods, are not needed. It is based on chemically intuitive tight-binding approximation to the quantum mechanical electronic structure[48–51] with the electronic degrees of freedom coarse-grained into a many-body interatomic potential that reflects correctly the angular character of bonding. This aspect of bonding can be very significant when the bonding has a mixed metallic and covalent character.[52,53] Within the scheme, the Hellmann-Feynman theorem can be used to evaluate forces on the atoms and the computational effort scales linearly with the number of atoms in the system. This method, which employs an orthogonal TB basis and two-center bond integrals, has been implemented in the Oxford order-N package (OXON).[54] An important recent advancement of BOPs that significantly enhances their robustness, specifically the transferability to different situations, has been the introduction of the environment dependence of two-center bond integrals. This has been attained through the analytic screening function derived in Ref. 55 by starting from a non-orthogonal tight-binding representation and using BOP methodology to invert the overlap matrix. The resultant bond integrals are explicitly dependent on the local environment not only through the bond lengths but also through the bond angles. They are then fitted to reproduce accurately the values of the screened bond integrals that are obtained numerically from calculations employing the first principles tight-binding linearized-muffin-tin-orbitals (TB-LMTO) method.[56]

The BOPs have now been constructed for three elemental transition metals, titanium,[57] molybdenum[58] and iridium[59] as well as for Ti-Al alloys.[60] These potentials were employed extensively in studies of dislocations and led to a number of important findings. In the case of titanium the preference for the prism slip was explained.[61] The core structure of the $1/2\langle 111\rangle$ screw dislocation found using the BOP for molybdenum is in full agreement with DFT calculations[58,62,63] but differs from that obtained in studies using central-force potentials.[64–67] Furthermore, studies of the motion of screw dislocations in molybdenum revealed significance of stresses perpendicular to the slip direction on the onset of plastic deformation.[68,69] In iridium, unlike in any other FCC metal, two core structures for the screw dislocation have been found. Transformation between these two structures may lead to an exceptionally high rate of cross slip during plastic deformation and associated rapid increase in the dislocation density and strong local hardening. This may explain the unique phenomenon of brittle cleavage of iridium after extensive plastic deformation.[70] For TiAl, the compound crystallizing in the $L1_0$ structure, the BOP predicts energies of stacking-fault-like defects and dislocation core structures that agree with both experimental observations and *ab initio* calculations.[60,71]

In this paper we present the BOP for tungsten that has been developed similarly as the BOP for molybdenum.[58] Since the theoretical background of BOP, in particular implementation of the analytic screened bond integrals into the scheme, has been presented in detail in Ref. 58, we summarize in Sec. II only the main concept and some formulas that are necessary for the explanation of BOP construction and parameterization. An essential part of the development of interatomic potentials is the assessment of their reliability, in particular their transferability to environments other than those used in the fitting procedure. Such testing is presented in Sec. III and it comprises calculations that can be directly compared with *ab initio* DFT calculations and/or experiments. These are evaluation of energy differences between alternative crystal structures, investigation of deformation paths transforming the BCC structure to other structures, and calculations of phonon spectra and the vacancy formation energy. In Section IV we apply the constructed BOP

to study several representative extended defects, namely low-index surfaces, symmetric tilt grain boundaries and screw dislocations. Dislocation calculations involve investigation of the effect of applied shear stresses and analysis of the results in terms of γ-surfaces that characterize shearing along crystallographic planes.[26,65,72] Finally, in Section V we summarize the most important aspects of the BOP for tungsten and discuss its applicability in large-scale atomistic studies.

II. BOP FORMALISM AND PARAMETERIZATION

A detailed description of the bond-order potential formalism for transition metals and their alloys can be found in the recent literature.[54,58,60,73] Since the currently developed BOP for W is analogous to that previously developed for Mo[58] we present in the following only the basics of the BOP theory necessary for the definition and understanding of model parameterization. For a more detailed description of the scheme and the fitting procedures the reader is referred to Ref. 58.

In the BOP formulation the total binding energy is composed of three terms:

$$E = E_{bond} + E_{env} + E_{pair}. \tag{1}$$

E_{bond} is the attractive bond energy, E_{env} is a purely repulsive environment-dependent term that originates from the repulsion due to the valence s- and p-electrons being squeezed into the ion core regions under the influence of the large covalent d-bonding forces, and E_{pair} is a pairwise term that includes all remaining interactions not explicitly covered by the two preceding terms.

Within the two-center, orthogonal TB model the bond energy can be partitioned into a sum of contributions from individual $i-j$ bonds, E^{ij}_{bond}, where

$$E^{ij}_{bond} = 2\sum_{\alpha\beta} H_{i\alpha,j\beta}\Theta_{j\beta,i\alpha}. \tag{2}$$

The prefactor 2 in Eq. 2 accounts for spin degeneracy and $H_{i\alpha,j\beta}$ and $\Theta_{j\beta,i\alpha}$ are the Hamiltonian and bond-order matrix elements, respectively. They are both associated with individual bonds between atomic orbitals α and β centered on corresponding atoms i and j. The Hamiltonian matrix elements $H_{i\alpha,j\beta}$ are defined in terms of the usual two-center Slater-Koster bond integrals and their angular dependencies.[74] Since the cohesion of BCC transition metals is governed by d–d bonding, only d-electrons have been included explicitly into E_{bond} in our model. The validity of this approximation has been discussed and tested extensively; see, for example Refs. 40,41,75. The dominance of d-electron bonding is clearly seen from the s-, p- and d-projected densities of states presented in Fig. 1(a) that have been obtained using the TB-LMTO method[56] for BCC tungsten.

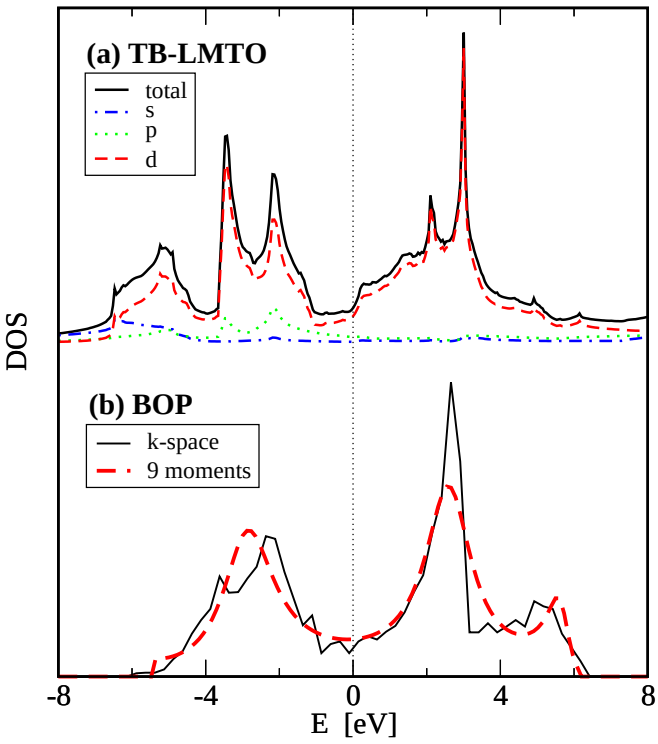

FIG. 1: Electronic densities of states of BCC W calculated by (a) TB-LMTO method and (b) the present parameterization using both the k-space TB and 9-moment BOP theory.

The dependencies of the three bond integrals ddσ, ddπ and ddδ, which enter the BOP model for W, on the interatomic distance have been obtained by first-principles TB-LMTO[55,56,76] and are presented in Fig. 2. Similarly as in other transition metals, magnitudes of the d-bond integrals decrease rapidly with increasing interatomic distance, and only first and second nearest neighbor (NN) contributions are significant in the BCC structure. The data in Fig. 2 also show that the TB-LMTO bond integrals display a marked discontinuity between the first and second shells for the ddπ and ddδ bond integrals. As discussed previously in Refs. 58 and 77, this is a result of the screening of the bond integrals by the local environment. The environment dependence of the bond integrals can be described within the BOP scheme as

$$\tilde{\beta}^{ij}_{\tau} = \beta_{\tau}(R_{ij})(1 - S^{ij}_{\tau}), \tag{3}$$

where $\tilde{\beta}^{ij}_{\tau}$ and β^{ij}_{τ} are the screened and unscreened bond integrals, respectively, and τ denotes the σ, π or δ bond. The many-body screening function S^{ij}_{τ} reflects the effect of the environment surrounding the bond $i-j$ on its strength and depends generally on the bond and overlap integrals between orbitals centered on atoms i and j and orbitals centered on neighboring atoms. The analytic form of the screening function has been derived from the non-orthogonal TB theory[55] and is described in detail in Ref. 58. In the current model the screening arising from the non-orthogonality of the orbitals is assumed to be

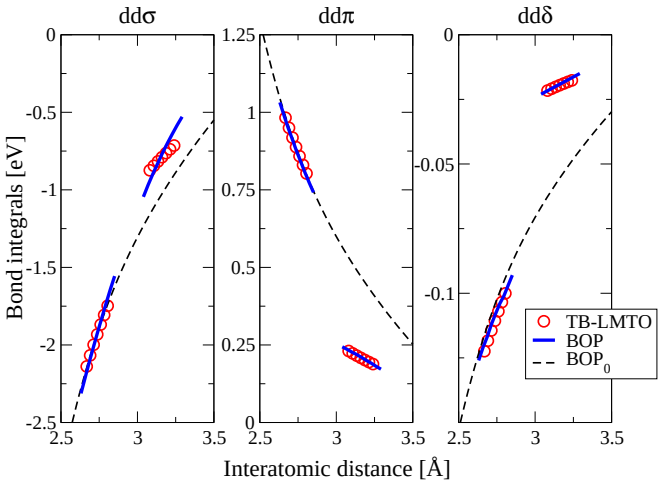

FIG. 2: Radial dependencies of $dd\sigma$, $dd\pi$ and $dd\delta$ bond integrals. Circles: Values calculated using TB-LMTO for the first and second nearest neighbors in BCC W with varying lattice parameter. Dashed curves: unscreened bond integrals. Full curves: screened bond integrals.

due to the s-valence electrons on the atoms surrounding the bond and requires therefore only additional parameterization of the sdσ bond and overlap interactions.

As in Ref. 58, dependencies on the interatomic distance of the unscreened bond, $\beta_\tau(R)$, and overlap, $O_\tau(R)$, integrals are represented by continuous pairwise functions of the generalized Goodwin-Skinner-Pettifor (GSP) form,[78] namely

$$\begin{aligned}\beta_\tau(R) =& \beta_\tau(R_0)\left(\frac{R_0}{R}\right)^{n_a} \\ & \times \exp\left\{n_b\left[\left(\frac{R_0}{R_c}\right)^{n_c} - \left(\frac{R}{R_c}\right)^{n_c}\right]\right\} \\ O_\tau(R) =& O_\tau(R_0)\left(\frac{R_0}{R}\right)^{n_a} \\ & \times \exp\left\{n_b\left[\left(\frac{R_0}{R_c}\right)^{n_c} - \left(\frac{R}{R_c}\right)^{n_c}\right]\right\},\end{aligned} \tag{4}$$

where n_a, n_b, n_c and R_c are fitting parameters. $\beta_\tau(R_0)$ and $O_\tau(R_0)$ are magnitudes of the first nearest-neighbor bond and overlap integrals in the BCC structure, respectively; the first NN distance in W, R_0, is equal to 2.74 Å. In order to guarantee that the bond and overlap integrals decrease smoothly to zero, the GSP function is employed for $R < R_1$ and is augmented with a polynomial of fifth order, given by Eq. (14) in Ref. 58, for $R_1 < R < R_{cut}$. The coefficients of this polynomial spline are computed on-the-fly so that the function, and its first and second derivatives are continuous at $R = R_1$ and zero at $R = R_{cut}$. The best choice of R_1 and R_{cut} was found to be the same for all the bond and overlap integrals, specifically 2.8 Å and 4.45 Å, respectively. The solid curves in Fig. 2 show the accuracy of the fit achieved by the analytic expression for the screened bond integrals. In order to assess the importance of the screening of the bond integrals, we have also constructed a bond-order potential without the screening, which is designated in the following as BOP_0. Corresponding values of the parameters entering the GSP functions for both BOP models are summarized in Table I.

Calculations of the screening function, the bond orders and the bond energies are complex and computationally demanding and have been done using the OXON package.[54] The bond-order matrix is evaluated under the assumption of local charge neutrality that is an excellent approximation for metallic systems. In order to assure a reliable description of local bonding in defective regions and, in general, in less ordered environments, nine moments of the density of states[41] are used in our calculations. This also guarantees that all the important features of the density of states (DOS) are correctly reproduced. As is shown in Fig. 1(b), both the bimodal behavior and the pseudogap of the exact k-space DOS are matched well by the nine-moment BOP approximation. Additional parameters (e.g. the number of d-electrons, fictitious electronic temperature) which are necessary for calculation of the bond energy in Eq. 2 are the same as in Ref. 58.

The second step in the construction of the BOP is fitting of the repulsive environment-dependent term E_{env}. It is described by a screened Yukawa-type potential:[79,80]

$$E_{env} = \frac{1}{2}\sum_{i,j\neq i}\frac{B}{R_{ij}}\exp\Big[-\lambda_{ij}(R_{ij}-2R_{core})\Big], \tag{5}$$

where R_{core} is the core radius and $\lambda_{ij}= (1/2)(\lambda_i + \lambda_j)$. The screening exponent λ_{ij} is dependent on the environment of atoms i and j. We model this environment dependence through an embedded-atom-type expression by writing:

$$\lambda_i = \lambda_0 + \left[\sum_{k\neq i} C\exp(-\nu R_{ik})\right]^{1/m}, \tag{6}$$

where λ_0 (the unscreened value of the exponent), C, ν and m are all adjustable parameters. These parameters are determined by fitting the experimental value of the Cauchy pressure $C_{12} - C_{44}$ in BCC tungsten since the bond part alone does not lead automatically to the correct value. Similarly as in the case of the bond integrals, a smooth polynomial cut-off tail was introduced in the environment-dependent term, namely for the embedding exponential function in Eq. 6. For $R_{tail} < R < R_{cut}$, this function is augmented by a polynomial of fifth order to ensure a smooth decay to zero. The values of all parameters of this repulsive term are listed in Table II.

The final contribution to the binding energy is a pairwise interaction

$$E_{pair} = \frac{1}{2}\sum_{i\neq j} V(R_{ij}). \tag{7}$$

TABLE I: Parameters of the GSP function for the bond and overlap integrals.

	R_c [Å]	$\beta_\tau(R_0)$ [eV]	$O_\tau(R_0)$	n_a	n_b	n_c
BOP						
ddσ	1.873	-1.800	0.0442	0.179	0.179	4.426
ddπ	1.015	1.000	-0.0352	0.000	1.000	1.274
ddδ	0.500	-0.182	0.0253	0.000	1.000	1.000
sdσ	0.750	-1.400	0.1650	0.000	1.000	1.000
BOP_0						
ddσ	1.000	-1.9167	–	4.0	4.0	0.05
ddπ	1.000	0.8801	–	4.0	4.0	0.05
ddδ	1.000	-0.1037	–	4.0	4.0	0.05

Values of parameters R_1 and R_{cut} are equal to 2.8 Å and 4.45 Å, respectively, for all integrals.

TABLE II: Parameters of the repulsive environment-dependent term of BOP_0 and BOP.

	B [eV Å]	R_{core} [Å]	λ_0 [Å^{-1}]	C [Å^{-m}]	ν [Å^{-1}]	m	R_{tail} [Å]	R_{cut} [Å]
BOP	101.5	1.0	3.0	200.0	1.8	2.0	3.30	4.45
BOP_0	15.0	1.0	2.0	110.0	1.5	2.0	3.30	4.40

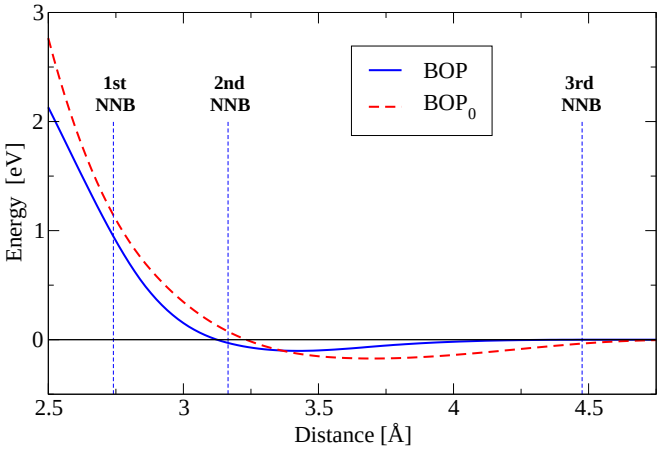

FIG. 3: Pair potential scaling for BOP and BOP_0 with marked distances of first, second and third nearest neighbors in the BCC lattice.

$V(R_{ij})$ is a pair potential and, similarly as in previous studies,[58–60,81] it is taken as a sum of cubic splines:

$$V(R_{ij}) = \sum_{k=1}^{4} A_k (R_k - R_{ij})^3 H(R_k - R_{ij}), \qquad (8)$$

where $H(x)$ is the Heaviside step function. The node points R_k and coefficients A_k are used as fitting parameters. This functional form of the pair potential assures that $V(R_{ij})$, as well as its first and second derivatives, are everywhere continuous and equal to zero at the cut-off distance R_1. The parameters of the pair potential are obtained by fitting two elastic constants that remain after fixing the Cauchy pressure, the cohesive energy and the equilibrium lattice parameter. The values of the node points, R_k, and coefficients, A_k, that have been found using this procedure are summarized in Table III for both BOP and BOP_0 and the corresponding pair potentials are plotted in Fig. 3.

Both pair potentials are repulsive at short distances, since they mainly represent the overlap repulsion and the electrostatic interaction between atoms, but provide a weak attraction beyond second NN of the BCC lattice. This can be justified when considering that the bonding and environmental repulsive parts of the cohesion do not include bonding due to s- and p-electrons and the hybridization effects, which may provide additional attractive contributions to the total energy. However, it should be noted that the attraction described by the pair potential is not based on any rigorous analysis but results from the fitting.

The five fundamental properties of the ground state BCC structure, which have been used to fit the potentials are summarized in Table. IV.

III. VALIDATION OF THE POTENTIAL

In order to assess the reliability of constructed potentials we performed a series of calculations and compared their results with results of *ab initio* calculations and/or available experimental data. Such validation is important for the use of potentials in studies of extended defects since they are fitted to only a minimal number of empirical and *ab initio* data for the ground state BCC structure and do not embody any implicit information about any other configurations.

We also include in our testing results of the central-force Finnis-Sinclair potential parameterized for W by Ackland and Thetford[84]. Even though it is known that the central-force potentials cannot describe adequately bonding in transition metals they can still serve as a

TABLE III: Parameters of the pair potentials for BOP_0 and BOP.

	BOP		BOP_0	
i	R_i [Å]	A_i [eV Å^{-3}]	R_i [Å]	A_i [eV Å^{-3}]
1	4.60	−0.101453949537	4.80	−0.254933510570
2	3.75	1.381881663730	4.60	0.531685598475
3	3.10	4.111472692380	3.60	0.961779038168
4	2.85	−12.634040533950	2.90	5.949929825811

TABLE IV: Fundamental properties of the ground state BCC structure used for fitting of BOPs: lattice parameter a [Å], cohesive energy per atom [eV] and elastic moduli [GPa] (from Refs. 82,83).

a	E_{coh}	C_{11}	C_{12}	C_{44}
3.1652	8.90	522.4	204.4	160.6

valuable tool provided that their limitations are well understood. Due to their simplicity and high computational efficiency these potentials can be used in calculations that can quickly probe a large number of atomic arrangements and help thus to identify critical configurations. However, a careful investigation of the structure and properties of these configurations has to employ more reliable methods. Understanding limits of simple potentials is also crucial for eventual coalescence of BOP and central-force schemes into a robust multiscale framework.

The characteristics that have been included in testing are the energies of several alternative crystal structures, the variation of the energy with structural transformations that correspond to four distinct deformation paths, the phonon dispersion curves for three low-index directions, and the vacancy formation energy.

A. Alternative crystal structures

The primary requirement on the constructed potentials is the stability of the ground state BCC structure relative to other crystal structures. This has been tested by calculating energies of several high-symmetry structures, namely A15, FCC, HCP (with ideal c/a ratio), and simple cubic (SC), as functions of their densities. The calculations were performed using both the screened BOP and unscreened BOP_0 potentials as well as the FS potential and a DFT method.[85–88] The calculated energy vs. volume per atom dependencies are shown in Fig. 4. (We did not include in Fig. 4 results for the HCP structures because they almost coincide with those for the FCC structure and are difficult to discern.)

Figs. 4(a) and (b) show that not only is the BCC structure most stable in the whole range of investigated volumes but that both BOP parameterizations reproduce well the DFT results for the FCC, HCP and SC structures even though the only fitted quantities were the cohesive energy and elastic moduli of the BCC structure at its equilibrium volume. Similarly as in the case of Mo[58] and Ir[59], the transferability of BOPs to the A15 structure is less satisfactory and the energy of this structure is overestimated when compared with *ab initio* results. In order to gain an insight into the origin of this discrepancy, we separated the structural energy differences of the three lowest energy structures, calculated at the BCC equilibrium volume per atom, into two parts: The bond contribution E_{bond}, shown in Fig. 5(a), and the sum of contributions from E_{env} and E_{pair}, shown in Fig. 5(b). Fig. 5(a) also contains the total energy differences calculated by DFT. It is obvious from this figure that for both BOPs the E_{bond} contribution alone predicts the correct order of structural stability. Although the bond contributions systematically overestimate the total energy differences given by DFT, they follow closely the DFT trend. However, when the E_{env} and E_{pair} contributions, shown in Fig. 5(b), are added the structural order changes. While for the FCC and HCP structures these contributions are negative and compensate the bond part overestimate, for the A15 structure they are strongly positive and make the A15 structure less stable than FCC and HCP in disagreement with DFT results. Hence, this decomposition indicates that the errors in the prediction of the energy difference for the A15 structure are caused by the E_{env} and E_{pair} parts of the binding energy while E_{bond} describes the bonding in this structure quite correctly. Since the first NN separations in the A15 structure are very short (almost 10% shorter than in the BCC structure at the same volume) the errors originate most likely from excessive short-range repulsion.

As expected, calculations using the FS potential are not in agreement with DFT calculations. Since this potential is based on the second-moment approximation of the density of states it is unable to predict the structural differences of transition metals[41] and the stability of the BCC structure is instead artificially imposed by fitting. The inability of the second-moment scheme to describe the relative stability is most evident in Fig. 5(a) where the FS bond contributions are almost identical for all three structures. Consequently, when using the FS potential, the BCC structure is the lowest energy structure only in a small interval around its equilibrium volume per atom (see Fig. 4(c)). For higher densities the FCC structure becomes more stable, while for lower densities A15 and FCC have lower energies than BCC. This test clearly demonstrates that the FS potential is applicable only to situations in which the density does not deviate

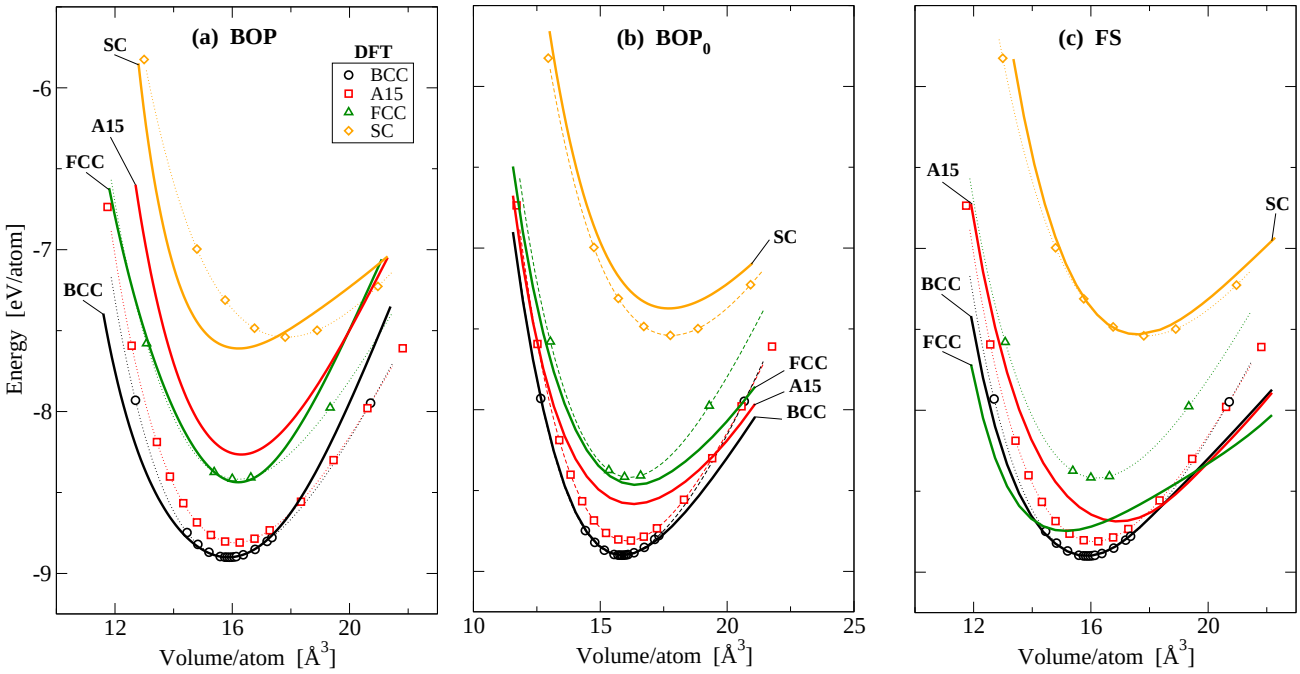

FIG. 4: (Color online) Energy vs. volume per atom dependencies for high-symmetry structures calculated by (a) BOP, (b) BOP_0, (c) FS potential[84] (full lines). DFT results are shown as symbols connected by dotted curves to guide the eye (DFT data were normalized to the experimental cohesive energy and volume of BCC W).

significantly from that of the ideal BCC crystal.

B. Deformation paths

Another important test, related to the previous one, is the investigation of transformation paths. This test probes not only the high symmetry structures but also distorted configurations that are encountered when one structure transforms into another. Furthermore, the deformation paths provide additional information about ideal tensile and shear strengths of materials.[89–91] Four such paths, tetragonal, hexagonal, orthorhombic and trigonal,[91–93] were investigated. A detailed definition of the tetragonal, hexagonal and trigonal paths can be found in Ref. 93 and the orthorhombic path is defined below. Each such path can be characterized by a parameter, p, and the energy was calculated as a function of this parameter using BOP, BOP_0, DFT,[86,94,95] and FS potentials. The results for all four paths are shown in Fig. 6. Both BOP_0 and BOP reproduce the *ab initio* data quite closely and thus this analysis does not reveal any substantial influence of the screening of the bond integrals. Nevertheless, these calculations again highlight the importance of directional bonding through large deviations of FS results from the DFT data.

Fig. 6(a) shows the most common transformation path, the tetragonal path, which is also known as the Bain path.[96] Along this path the body-centered tetragonal (BCT) structure is stretched at constant volume along the [001] axis and the high symmetry BCC and FCC structures are obtained as special cases. The parameter p is in this case the c/a ratio where a is the lattice parameter in the [100] and [010] directions and c in the [001] direction, with $c/a = 1$ corresponding to the BCC and $c/a = \sqrt{2}$ to the FCC structure. The tetragonal deformation is also directly linked with evaluation of the ideal strength for tensile loading along the [001] axis. Since, owing to the symmetry, the BCC and FCC structures correspond to the minimum and maximum of the energy, respectively, the inflection point between the two structures on the path determines the ideal tensile strength. Previous DFT calculations of Šob et al.[92] and Roundy et al.[97] identified the $\langle 001 \rangle$ axis as the weak direction in tension and the $\{001\}$ planes as the cleavage planes. Calculations employing BOPs follow closely the DFT ones indicating that both the ideal tensile stress and strain will be in a good agreement with the *ab initio* values. In contrast, the FS potential predicts the FCC structure not as a local maximum but as a saddle point with energy more than a factor of two smaller than the FCC energies obtained by the other methods. Additionally, the BOPs and DFT calculations show that if the structure is deformed beyond the FCC local maximum it reaches another local minimum for c/a around 1.7. It was found recently by Luo et al.[91] that this BCT structure is closely related to a tetragonal saddle-point structure which determines the ideal shear strength for the $\{211\}\langle 111 \rangle$ and $\{011\}\langle 111 \rangle$ slip systems. This BCT structure can be accessed also directly via the orthorhombic deformation

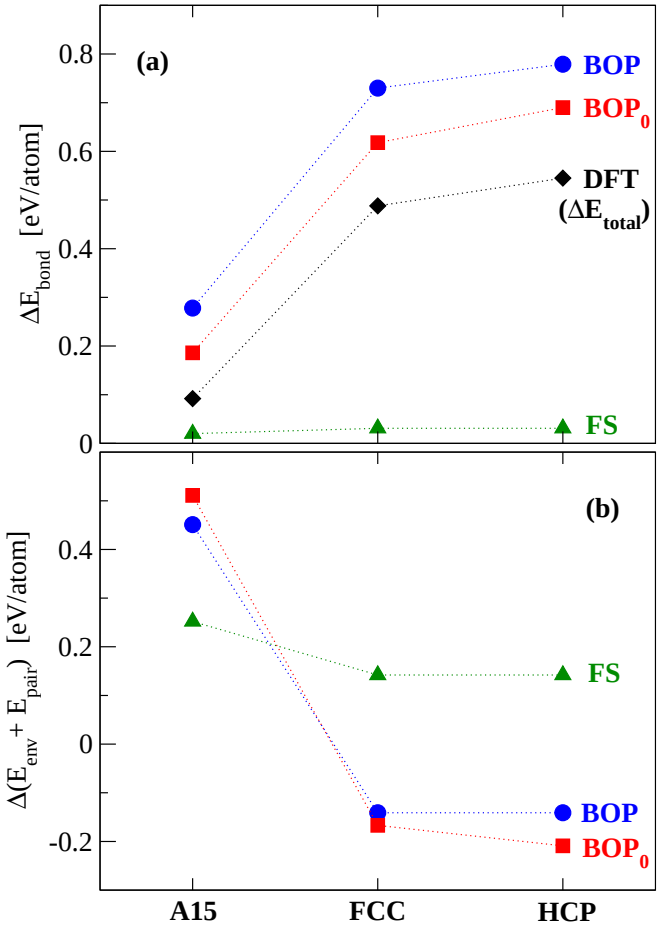

FIG. 5: Comparison of E_{bond} (a) and $E_{env} + E_{pair}$ (b) contributions to the structural energy differences between various close-packed structures and the BCC structure, calculated by BOP, BOP_0 and FS. Fig. (a) also contains the total energy differences obtained from DFT calculations.

which can be regarded as a generalization of the Bain path.[91]

During the orthorhombic deformation the BCC structure is simultaneously stretched along the [001] direction and compressed in the [110] direction. In the coordinate system where x, y, and z axes are parallel to [110], [$\bar{1}$10], and [001] directions, respectively, the deformation can be described by the following Lagrangian strain tensor for large deformations

$$\begin{aligned} \varepsilon_{11} &= (p^{-1} - 1)/2 \\ \varepsilon_{33} &= (p - 1)/2 \\ \varepsilon_{22} &= \varepsilon_{12} = \varepsilon_{13} = \varepsilon_{23} = 0. \end{aligned} \tag{9}$$

The parameter p characterizing this path is equal to 1 for the initial BCC structure and 2 at the final point corresponding again to the BCC structure with the same lattice parameters as the initial structure. Along the path the crystal has a face-centered orthorhombic symmetry except for $p = \sqrt{2}$ that corresponds to a body-centered tetragonal structure with the c/a ratio of 1.682. For this path the energy vs p is displayed in Fig. 6(b) and it again shows an excellent agreement between DFT and BOPs results whereas the FS potential underestimates the energy substantially.

The hexagonal transformation path connects the BCC and HCP structures and it differs qualitatively from the other paths since it does not correspond to a purely homogeneous straining. Instead, it is a homogeneous deformation that preserves the atomic volume, combined with shuffling of alternate close packed atomic planes in opposite directions.[93] The results of calculations for the hexagonal path are presented in Fig. 6(c).

The trigonal path is also a deformation path between the BCC and FCC structures, similarly as the tetragonal path, but passing through the SC structure. Starting from the BCC structure, the trigonal path concurs with the homogeneous deformation corresponding to the extension along the [111] axis while keeping the atomic volume constant.[93] The calculated dependence of the energy per atom on the parameter p characterizing this path is shown in Fig. 6(d). It should be noted that the extrema for $p = 1$, 2 and 4, corresponding to different cubic structures, are dictated by the symmetry. However, the occurrence of the local minimum in the vicinity of $p = 3.5$ is specific to the material studied. For the FCC structure the energy then reaches a saddle point. All these features of the trigonal deformation path are correctly reproduced by BOP potentials. We should note here again that in contrast to *ab initio* and BOP, the FS potential leads to a qualitatively different result – it gives only one local minimum for the trigonal path, corresponding to the FCC structure.

C. Phonon spectra

A complementary test to the investigation of the transformation paths that lead to large deformations of the lattice is calculation of phonon spectra where small atomic vibrations around the equilibrium lattice positions are probed. We computed dispersion curves for three high symmetry directions in the Brillouin zone of the BCC lattice using the method of frozen phonons[98] and compared them with experimental data.

The frozen phonons calculations were performed for several displacements in the range $\pm 0.02a$, for which we presume that the harmonic approximation holds. The phonon frequencies were then calculated by fitting the energy versus displacement data by a polynomial of second order using the least squares method. The results for both BOP and BOP_0 are presented in Fig. 7 together with experimental data from inelastic neutron scattering measurements.[99]

Despite some minor quantitative discrepancies, the agreement is very satisfactory for the [100] and [111] directions and both potentials. However, for BOP_0 the longitudinal (L) and transverse (T2) (polarization along [001]) phonons near the zone edge in the [110] direction

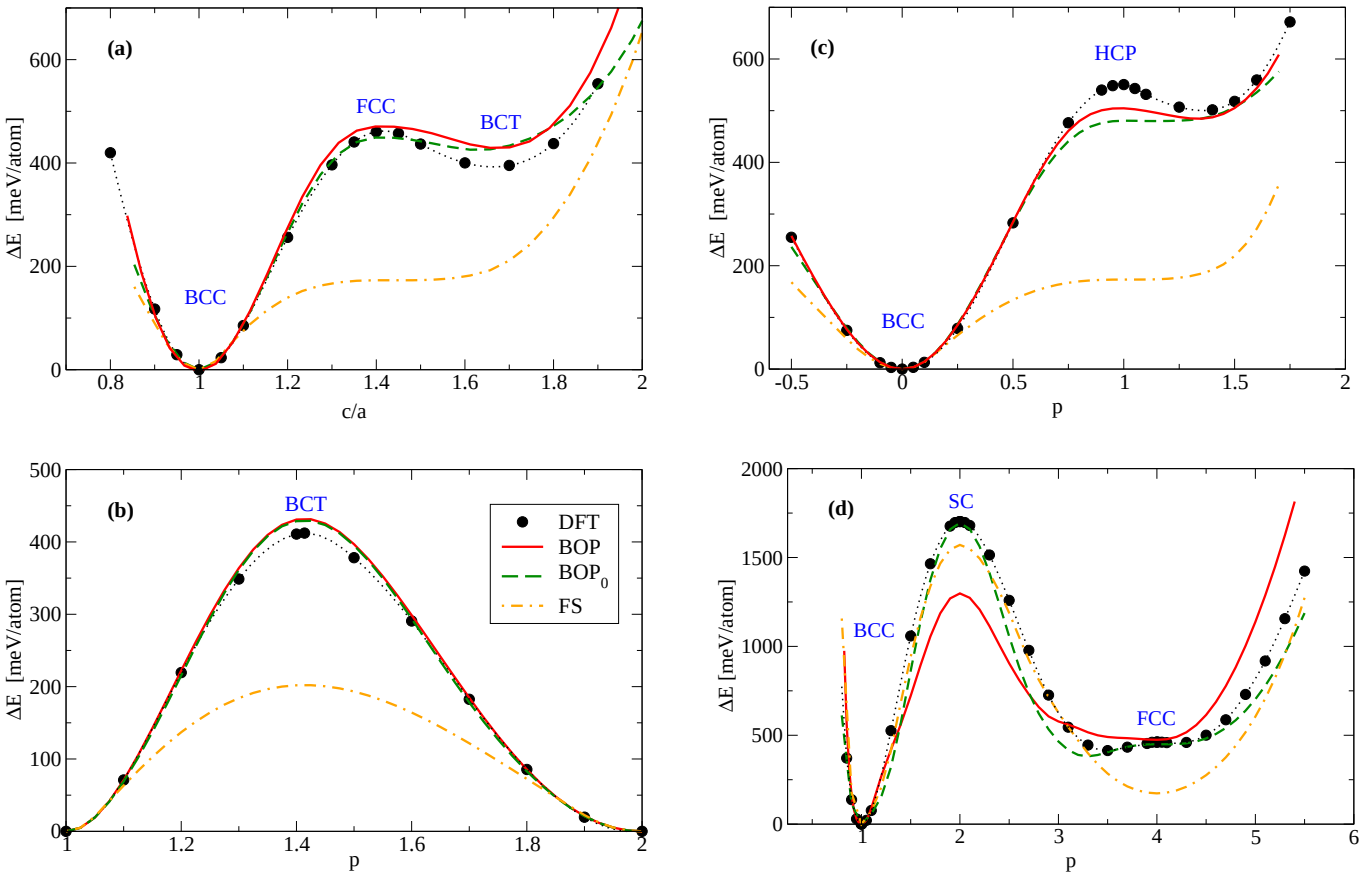

FIG. 6: (Color online) Energy per atom relative to the energy of the BCC lattice for the tetragonal (a), orthorhombic (b), hexagonal (c), and trigonal (d) deformation paths calculated by BOP, BOP_0, FS and DFT.

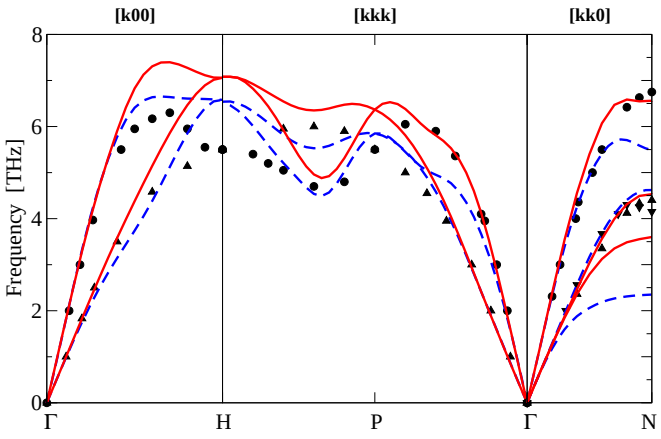

FIG. 7: Phonon dispersion curves for three high symmetry directions. Dashed and full curves represent results calculated by BOP_0 and BOP, respectively; symbols show experimental data.[99]

are much softer than experiment shows. When using the BOP with screened bond integrals the frequency of the T2 N-phonon mode increases significantly. Changes of the remaining two modes, while not so dramatic, also lead to dispersion curves that are closer to the experimental ones.

The problem of too soft N-point phonons in Mo and W is common in semi-empirical TB schemes.[100] It is therefore desirable to ascertain the underlying physical reason for the large improvement when the screening of bond integrals is introduced. As mentioned earlier, in the case of BOP_0 the second nearest neighbor $dd\pi$ and $dd\delta$ bond integrals are not represented with sufficient precision by simple scaling functions owing to the evident discontinuity between the first and second nearest neighbors. This is critical for the values of the second nearest neighbor force constants, which strongly influence the phonon spectra. Indeed, it was shown by Foiles[100] that it is the fourth moment of the density of states, i.e. the moment which links the second nearest neighbors, that affects the behavior of phonons in the [110] direction most profoundly. Hence, when the screening is introduced and the $dd\pi$ and $dd\delta$ bond integrals are reproduced with much higher precision, the accuracy of the phonon spectra improves.

When testing the constructed potentials the effect of screening is most dramatic for the case of Γ-N branch of the phonon spectrum. In the case of BOP_0 the longitudinal (L) and transverse (T2) phonons are appreciably softer than experiments suggest, particularly near the

N point. This is very significant for atomistic modeling of extended crystal defects. Low, or in the worst case imaginary, phonon frequencies may affect such simulations significantly and even lead to physically incorrect results if similar displacements occur within these defects. The lattice may deform too easily in the directions of soft phonons and this might induce unphysical relaxations and/or structural transformations. This danger is obviously much smaller for BOP than for BOP_0.

D. Vacancy

We modeled the vacancy using a cubic supercell of the size $3a \times 3a \times 3a$, where a is the lattice parameter, containing a total of 53 atoms, and using periodic boundary conditions. The convergence of the vacancy formation energy with the system size has been verified for supercells of sizes $4a \times 4a \times 4a$ and $5a \times 5a \times 5a$ giving almost identical results. The atomic configuration was fully relaxed under the condition of constant volume but we found, in accordance with DFT first principles calculations,[101] that the structural relaxation decreases the total energy only marginally. The vacancy formation energies calculated by FS, BOP and BOP_0 are presented in Table V. In the case of the FS potential the vacancy formation energy is in fact a fitted quantity and thus it agrees closely with both the results of first principles calculations and experimental data. The formation energy obtained using BOP_0 lies also within the range of available *ab initio* and experimental results (from Refs. 100,102 and references therein) while the screened BOP slightly overestimates the formation energy.

It is interesting to compare our results with those of other TB studies (see Table V). While another simple d-TB model,[101] similar to our unscreened BOP_0, predicts the vacancy formation energy in an excellent agreement with DFT calculations, a more sophisticated spd-TB model[103] overestimates it by almost a factor of two. This suggests that predictions of the vacancy formation energy can vary significantly even for closely related models. It has been shown[101] that in simple TB schemes the vacancy formation energy depends to the first order only on the ratio between the magnitude of the bond integrals and the magnitude of the repulsive pair interactions and can be easily adjusted. In more complicated schemes, such as spd-TB or screened BOP, the vacancy formation energy is determined from a subtle interplay of more contributions and a larger scatter of values is therefore likely unless the defect is included in the fitting database.

TABLE V: Vacancy formation energies (all values are in eV).

	E^f_{vac}
FS	3.64
BOP_0	3.83
BOP	4.30
d-TB[a]	3.56
spd-TB[b]	6.13
DFT[c]	3.3 – 3.8
Exp[c]	3.5 – 4.1

[a] See Refs. 101
[b] See Refs. 103
[c] See Refs. 100,102 and references therein.

E. Transferability and its limitations

It is obvious from the previous subsections that the constructed BOPs cannot be expected to reach the accuracy of the first-principles calculations but they provide a reliable approximation for description of atomic interactions in W. The transferability of any semiempirical model is the key issue in atomistic modeling and it requires a close attention, especially if the model is to be applied to simulations of unknown configurations where a high confidence in its predictive power is essential. In the test cases presented in this paper we have sampled a wide range of configurations that provide a stringent test bed for the constructed BOPs and thoroughly verify their transferability.

Unlike many other empirical or semiempirical schemes (see e.g. Refs. 77,103) the BOP model is fitted to only five most fundamental properties of the equilibrium BCC structure. As we have already mentioned this is not only an important advantage for a straightforward and well defined fitting procedure but it also provides an opportunity to asses the predictive capability of our model for simple configurations or properties that are frequently included in more extensive fitting databases. It is commonly assumed that the reliability of a model increases with the size of the fitting database used for its construction. However, fitting of a broad variety of attainable quantities may lead to unphysical values of model parameters when the physical basis of the model is insufficient for precise evaluation of the quantities fitted. Furthermore, elaborate fitting strategies may conceal inadequacies of physical principles on which the model is based. Thus a small number of fitting parameters together with reliable tested transferability is the best measure of the physical accuracy of the model.

Both past and present experiences with construction of BOPs indicate that the current description of the short-range repulsion does not mimic the influence of environment with sufficient accuracy. Even though it is commonly assumed in TB models that all repulsive interactions can be described by a pairwise potential[104] the repulsive contribution has a many-body character[105] and in the present study it is described by the Yukawa type form. This environment-dependent term, which was originally introduced to remedy the problem of fitting negative Cauchy pressures,[79,80] still has a central-force form that may not be capable to describe fully the repulsive interactions in different environments. In fact, the inversion of the non-orthogonality matrix which

leads to the screening of bond integrals described by Eq. 3 yields a similar screening function for the pairwise overlap repulsion.[80,106] Such screening function depends not only on interatomic distances but also on bond angles but this has not yet been implemented into the BOP model. The inadequacy of the description of repulsive interactions makes the present BOP schemes unsuitable for simulations of atomic configurations where the short-range repulsion is dominant. The most prominent defects of this type are self-interstitals and interstitial impurities.[107,108] However, the short-range interactions play much less important role in the extended defects discussed in the next section and the BOPs are likely to provide not only qualitatively but also quantitatively accurate results, as already ascertained by the previous study of molybdenum.[58]

IV. EXTENDED DEFECTS

In this section we apply the constructed potentials to studies of low-index surfaces, symmetrical tilt grain boundaries (STGB) and dislocations. These planar and linear defects have a major influence on mechanical behavior of materials and their accurate modeling is of paramount importance.

A. Surfaces

It has been already mentioned in the Introduction that tungsten fails predominantly by brittle fracture when subjected to mechanical loading at temperatures lower than the room temperature.[8] In brittle materials the criterion for the mechanical instability of a crack is based on the balance between the crack driving force, known as the energy release rate, and the surface energy of new surfaces created by fracture.[109] Even though the crack propagation in metallic materials always involves other competing processes such as dislocation nucleation and emission, or lattice trapping effects,[7] the correct prediction of surface energetics remains an important prerequisite for successful atomistic studies of fracture.

We have investigated properties of three low-index surfaces – (110), (211) and (100). The surface energies of these three relaxed unreconstructed surfaces are presented in Table VI. These results indicate that both BOP models give a correct ordering of the surface energies and that the BOP provides an improved agreement with DFT results and experimental values when compared with BOP_0. In contrast, surface energies obtained using the FS potential are both too small and incorrectly ordered.

Table VI also shows that the first (d_{12}) and second (d_{23}) interlayer spacings in all relaxed surfaces are compressed and expanded relative to the bulk, respectively. The percentage change of the interlayer spacings decreases in the correct order $|\Delta d_{12}(211)| > |\Delta d_{12}(100)| > |\Delta d_{12}(110)|$ which is found generally for BCC transition metals and is related to surface roughness.[114] The effect of relaxation is smallest for the most close-packed (110) surface. This is in agreement with both experimental and theoretical studies which show that the environment of this surface does not differ significantly, both electronically and structurally, from the bulk and the surface does not undergo any reconstruction.[111,115] The (211) surface exhibits the most corrugated structure among the surfaces investigated and the energy of this surface is substantially lowered by relaxation. In the relaxed structure of this surface the atoms are displaced not only in the direction perpendicular to the surface but also laterally in the $[\bar{1}11]$ direction parallel to the surface. This is again in agreement with DFT calculations and experimental observations.[112] At low temperatures clean (100) surface of W exhibits a commensurate $c(2 \times 2)$ reconstruction which results from alternating lateral displacements of surface atoms along the $[\bar{1}10]$ direction. This reconstruction has been studied in great detail both theoretically and experimentally (for a review see Ref. 113). We found that both BOP models predict the reconstructed (100) surface to be more stable than the unreconstructed one with lateral shifts of the surface layer atoms of 0.24 and 0.16 Å for BOP_0 and BOP, respectively. These values agree very well with other theoretical and experimental data that range between 0.18 and 0.27 Å.[113] In contrast, the FS potential predicts the unreconstructed structure as most stable.

Even though the BOP models do not reach the accuracy of the DFT calculations, e.g. for magnitudes of some surface relaxations that depend sensitively on subtle changes of the electronic structure,[113] both BOP models are able to capture qualitative trends in the energetics and structure of tungsten surfaces.

B. Grain boundaries

The microstructure of polycrystalline materials has a profound effect on their mechanical properties. For instance, during drawing and swaging tungsten wires and also wires made from other BCC metals develop a pronounced $\langle 110 \rangle$ texture.[116,117] The drawn wires show a preferred orientation, in which the $\langle 110 \rangle$ direction is parallel to the wire axis, and they are composed of a large number of highly elongated and curved grains whose length exceeds significantly their diameter. In the case of tungsten, this fibrous microstructure significantly improves the mechanical properties of the wires and gives them an increased ductility and strength compared to annealed tungsten that is very brittle at room temperature. However, the large number of grain boundaries (GBs) makes the wires more prone to intergranular fracture since they hinder the motion of dislocations and residual stresses may be more easily relaxed by decohesion along the GBs than by plastic deformation.[117] Knowledge of structure and energetics of GBs is therefore an

TABLE VI: Surface energies (in $\mathrm{mJ\,m^{-2}}$) and interlayer relaxations (in %) for unreconstructed relaxed low-index surfaces.

	(110)			(211)			(100)		
	$E_{surf}^{relaxed}$	Δd_{12}	Δd_{23}	$E_{surf}^{relaxed}$	Δd_{12}	Δd_{23}	$E_{surf}^{relaxed}$	Δd_{12}	Δd_{23}
FS	2575	-0.5	$+0.1$	3046	-4.8	$+1.1$	2924	-0.7	-0.6
BOP_0	2364	-0.4	$+0.3$	2588	-14.8	$+6.5$	3152	-3.2	$+0.3$
BOP	2604	-1.0	$+0.6$	3003	-7.9	$+2.1$	3805	-2.5	-0.4
DFT[a]	4005	-3.6	$+0.2$	4177	-	-	4635; 4780	-6 ± 0.5	0.5 ± 0.5
Exp[a]	3265; 3675	-2.7 ± 0.5	0.0 ± 0.3	-	-12.4	$+9.0$	-	$-6, -4 \pm 10$	-

[a]See Refs. 110–113 and references therein.

TABLE VII: Energies of several GBs (in $\mathrm{mJ\,m^{-2}}$). For the $\Sigma3(112)$ GB, energies of both the reflection (R) and isosceles (I) structures are shown.

	$\Sigma3(112)$		$\Sigma3(111)$	$\Sigma5(310)$	$\Sigma5(210)$
	(R)	(I)			
FS	395	461	2364	1807	2151
BOP_0	780	762	2398	1769	2477
BOP	1000	1004	3284	2718	3023
DFT	703	745	3196	2235	2781

important prerequisite for studies of dislocation-GB interactions or intergranular fracture.

We computed structures and energies of four symmetrical tilt GBs. The calculated energies of these GBs are presented in Table VII. One of the most studied GBs in the BCC metals is the $\Sigma3(112)$ STGB associated with the process of low temperature deformation twinning. The atomic structure of this boundary has been investigated extensively both theoretically and experimentally in various materials (see e.g. Ref. 118 and references therein). Both atomistic simulations and transmission electron microscopy observations have revealed existence of two possible translation states of this GB that are energetically almost degenerate. In one of them, there is no relative displacement of the two grains away from the exact coincidence and the mirror symmetry across the boundary plane is preserved. This is so-called "reflection" structure. The second structure does not possess the mirror symmetry with respect to the boundary plane and the upper grain is displaced with respect to the lower grain parallel to the boundary plane by the vector $1/12[11\bar{1}]$. The corresponding structure is called "sheared" or "isosceles".[119,120] Table VII shows that results for W are very much the same as the results of previous DFT calculations for Mo,[118] namely that the reflection structure is more stable and that the energy difference between the reflection and isosceles structures is very small. Both BOPs as well as the FS potential correctly predict the very small energy difference between the two translation states but the magnitude and even the sign of the difference are not reproduced accurately. Hence, the present results support the conclusion of Ref. 118 that it is beyond the predictive power of semi-empirical models to capture quantitatively such subtle energy differences. It should be noted, however, that the central-force FS scheme gives the GB energy almost factor of two smaller than the DFT and BOP calculations. This potential will therefore strongly favor twinning over other possible deformation mechanisms which may lead to unphysical results.[121] The reason is that in the twin boundary the separation of the first and second neighbors is the same as in the ideal crystal and thus in any central-force scheme only the third and more distant neighbors contribute to the energy. However, the bond angles are different even for the NN and the much higher energy predicted by BOPs therefore again emphasizes the importance of the directional bonding.

In the remaining three GBs both interatomic separations and bond angles are different from the ideal crystal for all neighbors, which is reflected in significantly higher energies than that of the deformation twin. Even though the BOP systematically overestimates the GB energies it gives the best agreement with the DFT calculations. This can be attributed to the most robust and accurate description of bonding.

C. Dislocations

It has been firmly established by many experimental and theoretical studies that lattice dislocations controlling the plastic properties of BCC metals are $1/2\langle111\rangle$ screw dislocations (for reviews see Refs. 13,14,20,21,23, 25,27). The reason is that their cores are non-planar and they are, therefore, much more difficult to move than dislocations of other orientations. However, the possibility to observe the atomic structure of the core of screw dislocations directly is very limited.[122,123] Consequently, it is an excellent topic for atomistic simulation and we present such study using the constructed BOPs.

A large number of atomistic simulations of dislocations in BCC metals have been made in the past using a broad variety of descriptions of interatomic interactions (for reviews see Refs. 23,124). In all these studies the core was found to spread into three $\{110\}$ planes, specifically $(\bar{1}01)$, $(0\bar{1}1)$ and $(\bar{1}10)$ for the $1/2[111]$ dislocation. Two types of the core were found that differ by invariance with respect to the $[10\bar{1}]$ diad. In one case the core is spread asymmetrically into these three planes and is not invariant with respect to this symmetry operation while in the

other case it is invariant and spreads symmetrically.[67] Which of the core structures is found depends on the material but both types have been found for nominally the same metal when using different descriptions of interatomic interactions. For example, for molybdenum, calculations employing FS potentials,[65,67] as well as calculations employing potentials derived from generalized pseudopotential theory,[125,126] showed the asymmetrical configuration. In contrast, the symmetrical configuration was found in recent DFT calculations[33,62,63,127] as well as in calculations employing the recently constructed BOP for molybdenum.[58]

γ-surfaces

Prior to the study of dislocation cores, it is always useful to investigate γ-surfaces for the planes into which the dislocation may be spreading. This theoretical construct represents the energy of a "generalized" stacking fault, formed by displacing the two parts of the crystal relative to each other along a crystal plane, as a function of this displacement. When calculating the γ-surface, relaxation perpendicular to the plane of the fault but not parallel to this plane is carried out. This concept was originally introduced when searching for possible stacking faults in BCC metals[72] and since then it has been employed extensively in atomistic studies of dislocations and stacking faults in a broad variety of materials.[20,23,24,26,65,126,128–134] Minima on such surfaces indicate possible metastable stacking faults and in BCC metals analysis of γ-surfaces for {110} planes can predict whether in a given material the core of the screw dislocations will be symmetrical or not.[65]

Using the constructed BOPs for W the γ-surface was calculated for the $(\bar{1}01)$ plane. Its overall profile is the same as that found in many previous calculations (see e. g. Ref. 124). The unrelaxed and relaxed [111] cross-section of this γ-surface is shown in Figs. 8(a) and (b), respectively. Besides the calculation employing the screened BOP we also present calculations made using BOP_0, FS potential, and results of our own DFT calculations[86] together with those of Frederiksen et al.[131]

While the agreement between the *ab initio* and BOP results is very good for both unrelaxed and relaxed γ-surfaces it is appreciably worse for BOP_0 and the worst for the FS potential. This suggests that, similarly as in molybdenum,[58] the agreement with *ab initio* calculations is the better the more accurately the dependence of the energy on bond angles is described. This dependence is included much more precisely in BOP than in BOP_0 owing to the screening of bond integrals which reflects the influence of environment.

As mentioned above, the γ-surface can be used to assess which of the two types of the core the screw dislocation is likely to adopt. Following Ref. 65, the symmetrical core, invariant with respect to the diad, is favored if $3\gamma(b/3) > 6\gamma(b/6)$ and vice versa for the non-

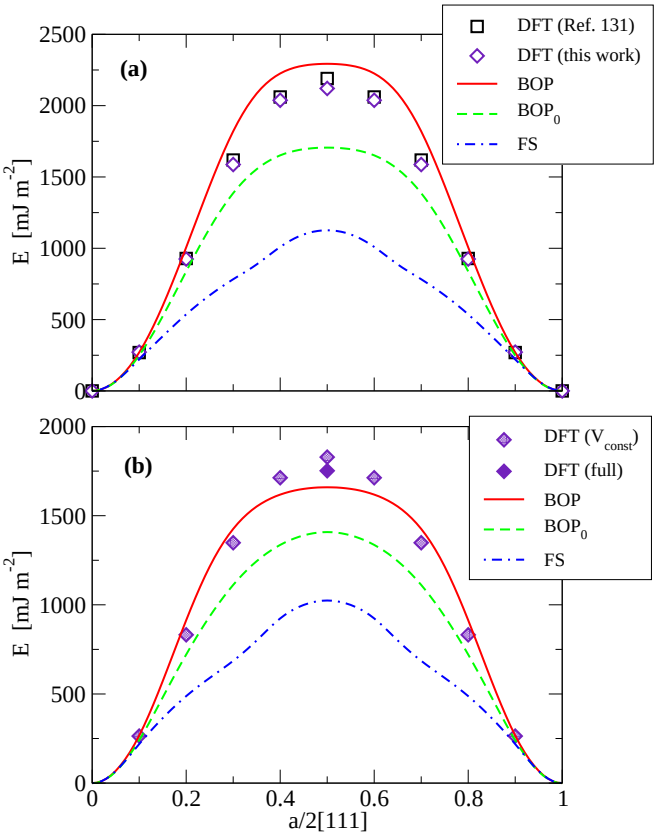

FIG. 8: Comparison of [111] cross sections of the {110} γ-surface; (a) unrelaxed, (b) relaxed. DFT calculations of the relaxed γ-surface were carried out at the BCC equilibrium volume (DFT(V_{const})); for the γ-surface maximum a full volume relaxation was also performed (DFT(ful)).

symmetrical core. Based on the γ-surface cross-sections shown in Fig. 8, the symmetrical core is favored for both BOP and BOP_0 and, indeed, this is what the computer modeling of the core structure shows. In fact, according to the *ab initio* calculations in Ref. 131 the symmetrical cores are likely to be found in all BCC transition metals. The reason is, presumably, the dominance of the d-bonding that invokes the strong dependence of the energy on bond angles, which leads to a rapid increase of the γ-surface with the displacement.[58] This aspect of bonding is well captured by BOP but not by the central-force FS potential.

Core structure and effect of externally applied stress

The core structure of the 1/2[111] screw dislocation in tungsten was studied using a molecular statics method, similarly as in earlier calculations.[58,65,66] The block of atoms was a parallelepiped with edges identified with coordinate axes as follows: x parallel to $[\bar{1}2\bar{1}]$, y parallel to $[\bar{1}01]$ and z parallel to [111]. The dislocation with its Burgers vector along the z direction was inserted in the

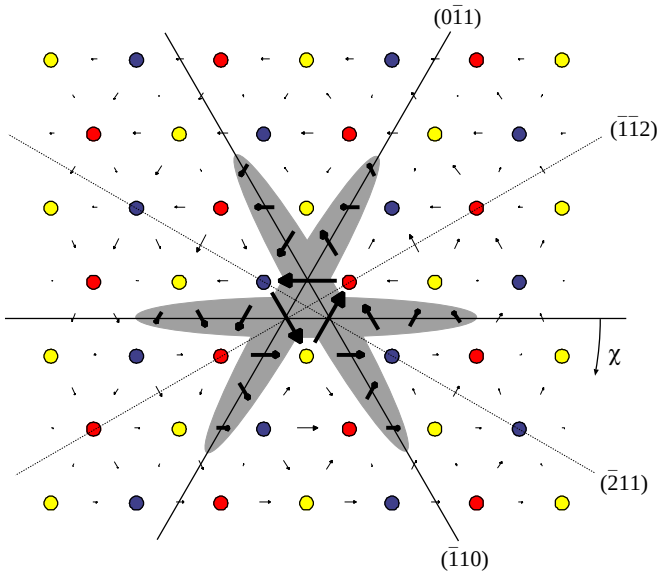

FIG. 9: Core structure of the 1/2[111] screw dislocation determined using BOP for tungsten. The atomic arrangement is shown in the projection perpendicular to the direction of the dislocation line (the [111] axis), and circles represent atoms within one period; their positions in three successive (111) planes are distinguished by shading. The [111] (screw) component of the relative displacement of the neighboring atoms produced by the dislocation is depicted as an arrow between them. The length of the arrows is proportional to the magnitude of these components. The arrows, which indicate out-of-plane displacements, are always drawn along the line connecting neighboring atoms and their length is normalized such that the longest arrow is equal to the separation of these atoms in the projection.

middle of the block by applying to all atoms in the block the displacement in accordance with the anisotropic elastic field of the dislocation.[18] Periodic boundary conditions were imposed in the z direction, i. e. parallel to the dislocation line. Perpendicular to the dislocation, in x and y directions, the block consisted of an active region in which all the atoms were fully relaxed and an inactive region where the positions of atoms were held fixed but the atoms interact with those in the active region. The active, fully relaxed region contained 711 atoms and the inactive region 858 atoms. The result of this study is shown in Fig. 9 using the usual differential displacement map, defined in the captions of this figure. The core is invariant with respect to the [10$\bar{1}$] diad and spreads symmetrically into the three {110} planes, as envisaged by analyzing the γ-surface. This core structure is virtually the same as that found for molybdenum when employing both the BOP[58] and a DFT method.[33,62,63]

Analysis of the core structure is only the first step in studies of dislocations. The ultimate goal is understanding their glide behavior under the effect of external loads. When applying a stress the elastic displacement field corresponding to this stress was evaluated using anisotropic elasticity theory and superimposed on the dislocation displacement field for the atoms in both the active and inactive regions. The relaxation then proceeded as in the unstressed case. Here we present a calculation of the effect of pure shear stress acting in the direction of the Burgers vector with various orientations of the maximum resolved shear stress plane (MRSSP). The orientation of the MRSSP is defined by the angle χ which this plane makes with the ($\bar{1}$01) plane. Owing to the crystal symmetry it is sufficient to consider $-30° \leq \chi \leq +30°$. However, it is important to note that orientations corresponding to positive and negative angles χ are not equivalent. For $\chi < 0°$ the nearest {112} plane, ($\bar{1}\bar{1}$2), is sheared in the twinning sense and for $\chi > 0°$ the nearest {112} plane, ($\bar{2}$11), is sheared in the anti-twinning sense. This relates to the well-known twinning-antitwinning asymmetry of the yield stress observed in many BCC metals and is usually regarded as the principal reason for the break-down of the Schmid law (for reviews see Refs. 13,14,21,23).

The calculations always started with the relaxed stress-free core structure. The applied shear stress in the [111] direction in the MRSSP was built up incrementally, in steps of $0.001\,C_{44}$ and full relaxation was carried out at every step. The stress at which the dislocation started to move was identified with the critical resolved shear stress (CRSS) for the dislocation glide at 0 K, i. e. the Peierls stress. At lower stresses the dislocation core transforms but these transformations are purely elastic in that the atomic structure returns to its unstressed configuration if the stress is removed. The calculations were carried out using both BOP and BOP_0 and the dependence of the CRSS on χ is displayed for both cases in Fig. 10. The difference between the results of the two potentials is significant. In the case of BOP the dislocation moved along the ($\bar{1}$01) plane for all angles χ. For the BOP_0 the dislocation also moved along the ($\bar{1}$01) plane for $\chi > 0°$ but for $\chi < 0°$ the dislocation moved by elementary steps on ($\bar{1}$01) and (0$\bar{1}$1) planes resulting in the glide along the ($\bar{1}\bar{1}$2) plane on average. This behavior is reflected in the CRSS vs χ dependence. For BOP_0 the twinning-antitwinning asymmetry is very pronounced, i. e. for positive χ the CRSS is significantly larger than for negative χ. In contrast, for the BOP the twinning-antitwinning asymmetry is negligible. Furthermore, since the slip plane is in this case always ($\bar{1}$01), the dependence of the CRSS on χ should have the form $1/\cos\chi$ according to the Schmid law. This dependence is shown as the dashed curve in Fig. 10 and it is seen that the Schmid law is obeyed closely for the pure shear in the slip direction by BOP but not by BOP_0.

However, the insignificant twinning-antitwinning asymmetry in pure shear does not imply that yielding in tungsten follows the Schmid law for any mode of loading. In fact, investigations of the effect of shear stresses perpendicular to the Burgers vector suggest strong tension-compression asymmetries and thus remarkable deviations from the Schmid law. These deviation are similar to

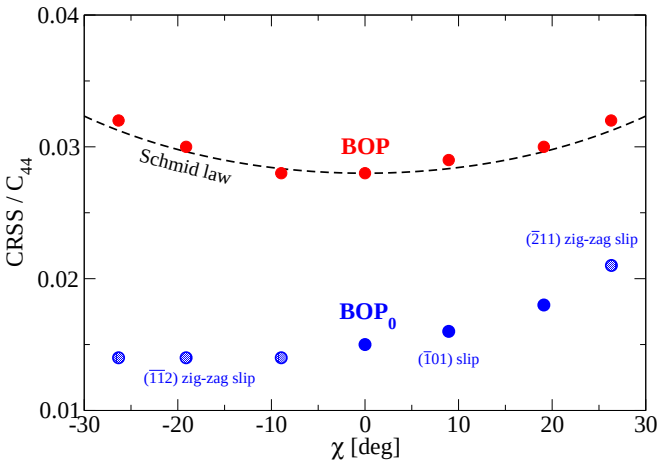

FIG. 10: Orientation dependence of the CRSS for loading by shear stress parallel to the slip direction and acting in the MRSSP characterized by the angle χ.

those found in molybdenum[69] in which the twinning-antitwinning asymmetry in pure shear in the slip direction, found when using the BOP, is significantly stronger than in tungsten.[58] The details of these studies will be published in a separate paper. Since experimental investigations of the yielding are usually made in tension, compression or employing more complex stress applications, such as indentation, there are no experimental data that would indicate whether in tungsten the twinning-antitwinning asymmetry is strong or weak for pure shear parallel to the slip direction. However, no experimental data suggest that the slip in tungsten is on {112} planes while {110} planes appear to be ubiquitous slip planes.[28,29,135–137] Hence, the BOP rather than BOP_0 appears to describe correctly the glide of screw dislocations in tungsten. This again underscores the importance of screening of bond integrals that leads to accurate description of angularly dependent bonding mediated by d-electrons.

V. CONCLUSIONS

In this work we have constructed and tested two variants of the bond-order potential for tungsten. The BOP scheme provides a real-space description of interactions between the atoms, which is based on the parameterized tight-binding approximation to the electronic structure and is therefore capable to treat mixed metallic and covalent bonding of transition metals and their alloys. This is crucial for atomic-level modeling of extended defects in these materials since the angular character of bonding may govern both their structures and properties. Considering the extensive testing presented in this paper we can conclude that the bond-order potential developed in this study is eminently suitable for atomistic studies of extended crystal defects in tungsten. This potential not only guarantees the stability of the BCC structure and reproduces a number of equilibrium properties but reflects accurately the very important feature of mixed metallic and covalent bonding, the dependence of the cohesive energy on bond angles arising due to the partially filled d-band. The screening of bond integrals implemented in the BOP model enhances considerably its transferability to structures that deviate significantly from the ideal BCC structure. Hence, atomistic studies employing this potential are likely to reveal correctly the structures and properties of those lattice defects, that induce changes in both bond lengths and bond angles while the short-range repulsions remain close to those in the ideal lattice. This is the situation encountered in many extended defects, such as surfaces, grain boundaries and dislocations, that control a variety of physical and mechanical properties. However, the present description of the short-range repulsion discourages the application of the constructed BOP to studies of point defects, in particular interstitials.

VI. ACKNOWLEDGEMENTS

This research was supported in part by the German Science Foundation, Grant no. Gu 367/25 (M.M.), by the U.S. Department of Energy, BES Grant no. DE-PG02-98ER45702 (R.G., A.G.B., V.V.), and by the EXTREMAT project, EURATOM and the United Kingdom EPSRC (D.N-M.). The authors gratefully acknowledge collaborations and fruitful discussions with David G. Pettifor, Ralf Drautz and Peter Gumbsch.

* Electronic address: matous.mrovec@iwm.fraunhofer.de

[1] A. T. Peacock, V. Barabash, W. Dänner, M. Rödig, P. Lorenzetto, P. Marmy, M. Merola, B. N. Singh, S. Tähtinen, J. van der Laan, et al., J. Nucl. Mater. **329-33**, 173 (2004).
[2] S. J. Zinkle, Phys. Plasmas **12**, 58101 (2005).
[3] H. Bolt, V. Barabash, W. Krauss, J. Linke, R. Neu, S. Suzuki, and N. Yoshida, J. Nucl. Mater. **329-33**, 66 (2004).
[4] I. V. Gorynin, V. A. Ignatov, V. V. Rybin, S. A. Fabritsiev, V. A. Kazakov, V. P. Chakin, V. A. Tsykanov, V. R. Barabash, and Y. G. Prokofyev, J. Nucl. Mater. **191-4**, 421 (1992).
[5] Q. Wei, K. T. Ramesh, B. E. Schuster, L. J. Kecskes, and R. J. Dowding, JOM **58**, 40 (2006).
[6] R. W. Margevicius, J. Riedle, and P. Gumbsch, Mater. Sci. Eng. A **270**, 197 (1999).
[7] P. Gumbsch, J. Nucl. Mater. **323**, 304 (2003).

[8] P. Gumbsch, J. Riedle, A. Hartmaier, and H. F. Fischmeister, Science **282**, 1293 (1998).
[9] P. Gumbsch, Mat. Sci. Eng. A **319**, 1 (2001).
[10] A. Hartmaier and P. Gumbsch, Phys. Rev. B **71**, 024108 (2005).
[11] J. Riedle, P. Gumbsch, and H. F. Fischmeister, Phys. Rev. Lett. **76**, 3594 (1996).
[12] J. W. Davis, V. R. Barabash, A. Makhankov, L. Plöchl, and K. T. Slattery, J. Nucl. Mater. **253-8**, 308 (1998).
[13] J. W. Christian, in *Proc. 3rd Int. Conf. on Reinstoffe in Wissenschaft und Technik* (Akademie-Verlag, Berlin, 1970), p. 263.
[14] J. W. Christian, Metall. Trans. A **14**, 1237 (1983).
[15] G. A. Cottrell, J. Nucl. Mater. **334**, 166 (2004).
[16] J. Friedel, *Dislocations* (Pergamon Press, Oxford, 1964).
[17] F. R. N. Nabarro, *Theory of Crystal Dislocations* (Clarendon Press, Oxford, 1967).
[18] J. P. Hirth and J. Lothe, *Theory of Dislocations* (Wiley-Interscience, New York, 1982).
[19] J. P. Hirth, Acta Mater. **48**, 93 (2000).
[20] V. Vitek, *Encyclopedia of Solid State Physics* (Elsevier, Oxford, 2005), p. 437.
[21] L. P. Kubin, Rev. Deform. Behav. Materials **4**, 181 (1982).
[22] V. Vitek, in *Dislocations and properties of real materials*, edited by M. Lorretto (The Institute of Metals, London, 1985), p. 30.
[23] M. S. Duesbery, *Dislocations in Solids* (Amsterdam, North Holland, 1989), vol. 8, p. 67.
[24] M. S. Duesbery and G. Y. Richardson, CRC Critical Reviews in Solid State and Materials Science **17**, 1 (1991).
[25] G. Taylor, Prog. Mater. Sci. **36**, 29 (1992).
[26] V. Vitek, Prog. Mater. Sci. **36**, 1 (1992).
[27] V. Vitek, in *Handbook of Materials Modeling Vol. I: Methods and Models*, edited by S. Yip (Springer, New York, 2005), p. 2883.
[28] D. Brunner and V. Glebovsky, Mater. Lett. **44**, 144 (2000).
[29] D. Brunner, Mat. Sci. Eng. A **387-9**, 167 (2004).
[30] S. Yip, *Handbook of Materials Modeling* (Springer, New York, 2005).
[31] A. H. Cottrell and D. G. Pettifor, eds., *Electron Theory in Alloy Design* (The Institute of Metarials, London, 1992).
[32] J. Hafner, Acta Mater. **48**, 71 (2000).
[33] C. Woodward, Mater. Sci. Eng. A **400**, 59 (2005).
[34] M. W. Finnis, Prog. Mater. Sci. **49**, 1 (2004).
[35] M. S. Daw and M. I. Baskes, Phys. Rev. B **29**, 6443 (1984).
[36] M. S. Daw, S. M. Foiles, and M. I. Baskes, Mater. Sci. Rep. **9**, 251 (1993).
[37] S. M. Foiles, MRS Bull. **21**, 24 (1996).
[38] G. J. Ackland, G. Tichy, V. Vitek, and M. W. Finnis, Phil. Mag. A **56**, 735 (1987).
[39] M. W. Finnis and J. E. Sinclair, Phil. Mag. A **50**, 45 (1984).
[40] J. Friedel, in *The Physics of Metals*, edited by J. M. Ziman (Cambridge University Press, Cambridge, 1969), p. 340.
[41] D. G. Pettifor, *Bonding and Structure of Molecules and Solids* (Oxford University Press, 1995).
[42] M. I. Baskes, Phys. Rev. B **46**, 2727 (1992).
[43] M. I. Baskes and R. A. Johnson, Model. Simul. Mater. Sci. Eng. **2**, 147 (1994).
[44] B. J. Lee and M. I. Baskes, Phys. Rev. B **62**, 8564 (2000).
[45] P. E. A. Turchi, A. Gonis, and L. Colombo, eds., *Tight-Binding Approach to Computational Materials Science*, vol. 491 (Materials Research Society, Pittsburgh, 1998).
[46] J. A. Moriarty, Phys. Rev. B **42**, 1609 (1990).
[47] J. A. Moriarty, Phys. Rev. B **49**, 12431 (1994).
[48] D. G. Pettifor, Phys. Rev. Lett. **63**, 2480 (1989).
[49] D. G. Pettifor, in *Many Atom Interactions in Solids*, edited by R. M. Nieminen, J. Puska, and M. Manninen (Springer, Berlin, 1990), vol. 48 of *Springer Reports in Physics*, p. 64.
[50] D. G. Pettifor and I. I. Oleinik, Comput. Mater. Sci. **23**, 33 (2002).
[51] D. G. Pettifor and I. I. Oleinik, Prog. Mater. Sci. **49**, 285 (2004).
[52] D. Pettifor, M. Aoki, P. Gumbsch, A. Horsfield, D. Manh, and V. Vitek, Mater. Sci. Eng. A **192/193**, 24 (1995).
[53] D. Nguyen-Manh, M. J. Cawkwell, R. Gröger, M. Mrovec, R. Porizek, D. G. Pettifor, and V. Vitek, Mater. Sci. Eng. A **400-401**, 68 (2005).
[54] A. P. Horsfield, A. M. Bratkovsky, D. G. Pettifor, and M. Aoki, Phys. Rev. B **53**, 1656 (1996).
[55] D. Nguyen-Manh, D. G. Pettifor, and V. Vitek, Phys. Rev. Lett. **85**, 4136 (2000).
[56] O. K. Andersen, A. Arcangeli, R. W. Tank, T. Saha-Dasgusta, G. Krier, O. Jepsen, and I. Dasgusta, in *Tight-Binding Approach to Computational Materials Science*, edited by L. Colombo, A. Gonis, and P. Turchi (Materials Research Society, Pittsburg, 1998), vol. 491, p. 3.
[57] A. Girshick, A. M. Bratkovsky, D. G. Pettifor, and V. Vitek, Phil. Mag. A **77**, 981 (1998).
[58] M. Mrovec, D. Nguyen-Manh, D. G. Pettifor, and V. Vitek, Phys. Rev. B **69**, 094115 (2004).
[59] M. J. Cawkwell, D. Nguyen-Manh, D. G. Pettifor, and V. Vitek, Phys. Rev. B **73**, 064104 (2006).
[60] S. Znam, D. Nguyen-Manh, D. G. Pettifor, and V. Vitek, Phil. Mag. A **83**, 415 (2003).
[61] A. Girshick, D. G. Pettifor, and V. Vitek, Phil. Mag. A **77**, 999 (1998).
[62] C. Woodward and S. I. Rao, Phil. Mag. A **81**, 1305 (2001).
[63] C. Woodward and S. I. Rao, Phys. Rev. Lett. **88**, 216402 (2002).
[64] V. Vitek, Cryst. Latt. Def. **5**, 1 (1975).
[65] M. S. Duesbery and V. Vitek, Acta Mater. **46**, 1481 (1998).
[66] K. Ito and V. Vitek, Phil. Mag. A **81**, 1387 (2001).
[67] V. Vitek, Phil. Mag. **84**, 415 (2004).
[68] V. Vitek, M. Mrovec, R. Gröger, J. Bassani, V. Lacherla, and L. Yin, Mater. Sci. Eng. A **387**, 138 (2004).
[69] R. Gröger and V. Vitek, Mater. Sci. Forum **482**, 123 (2005).
[70] M. J. Cawkwell, D. Nguyen-Manh, C. Woodward, D. G. Pettifor, and V. Vitek, Science **309**, 1059 (2005).
[71] C. Woodward and S. I. Rao, Phil. Mag. **84**, 401 (2004).
[72] V. Vitek, Phil. Mag. A **18**, 773 (1968).
[73] M. Aoki, D. Nguyen-Manh, D. G. Pettifor, and V. Vitek, accepted to Prog. Mater. Sci.
[74] J. C. Slater and G. F. Koster, Phys. Rev. **94**, 1498 (1954).
[75] C. D. Gelatt, H. Ehrenreich, and E. Watson, Phys. Rev. B **15**, 1613 (1977).
[76] H. Nakamura, D. Nguyen-Manh, and D. J. Pettifor, J. Alloys Comp. **306**, 113 (2000).
[77] H. Haas, C. Z. Wang, M. Fähnle, C. Elsässer, and K. M. Ho, Phys. Rev. B **57**, 1461 (1998).
[78] L. Goodwin, A. J. Skinner, and D. G. Pettifor, Europhys. Lett. **9**, 701 (1989).
[79] D. Nguyen-Manh, D. G. Pettifor, S. Znam, and V. Vitek,

in *Tight-Binding Approach to Computational Materials Science*, edited by P. E. A. Turchi, A. Gonis, and L. Colombo (Materials Research Society, Pittsburgh, 1998), vol. 491, pp. 353–358.
[80] D. Nguyen-Manh, V. Vitek, and A. P. Horsfield, Prog. Mater. Sci. (2006), doi:10.1016/j.pmatsci.2006.10.010.
[81] A. Girshick, Phd, University of Pennsylvania (1997).
[82] C. Kittel, *Introduction to Solid State Physics* (John Wiley, New York, 1986).
[83] P. Bujard, PhD Thesis, University of Geneve (1982).
[84] G. J. Ackland and R. Thetford, Phil. Mag. A **56**, 15 (1987).
[85] Our DFT calculations were carried out using a mixed-basis pseudopotential approach. The computational details for the pseudopotentials of W, the plane waves and localized functions in the mixed basis, the k-point meshes, etc. are like in the preceeding DFT studies of interfaces in W, Mo and other BCC metals in Refs. 87, 88, 118.
[86] B. Meyer, C. Elsässer, F. Lechermann, and M. Fähnle, Fortran90 Program for Mixed-Basis Pseudopotential Calculations for Crystals, Max-Planck-Institut für Metallforschung Stuttgart.
[87] T. Ochs, C. Elsässer, M. Mrovec, V. Vitek, J. Belak, and J. A. Moriarty, Phil. Mag. A **80**, 2405 (2000).
[88] T. Ochs, O. Beck, C. Elsässer, and B. Meyer, Phil. Mag. A **80**, 351 (2000).
[89] J. Pokluda, M. Černy, P. Šandera, and M. Šob, J. Comput. Aided Mater. Des. **11**, 1 (2004).
[90] C. R. Krenn, D. Roundy, J. W. Morris, and M. L. Cohen, Mater. Sci. Eng. A **319-321**, 111 (2001).
[91] W. Luo, D. Roundy, M. L. Cohen, and J. W. Morris, Phys. Rev. B **66**, 094110 (2002).
[92] M. Šob, L. Wang, and V. Vitek, Mater. Sci. Eng. A **234**, 1075 (1997).
[93] V. Paidar, L. G. Wang, M. Šob, and V. Vitek, Model. Sim. Mat. Sci. Eng. **7**, 369 (1999).
[94] M. Šob, private communication.
[95] P. Blaha, K. Schwartz, P. Sorantin, and S. B. Trickey, Comp. Phys. Comm **59**, 399 (1990).
[96] E. C. Bain, Trans. AIME **70**, 25 (1924).
[97] D. Roundy, C. R. Krenn, M. L. Cohen, and J. W. Morris, Phil. Mag. A **81**, 1725 (2001).
[98] K. Kunc, *Electronic Structure Dynamics and Quantum Structure Properties of Condensed Matter* (Plenum, New York, 1985).
[99] S. H. Chen and B. N. Brockhouse, Solid State Comm. **2**, 73 (1964).
[100] S. M. Foiles, Phys. Rev. B **48**, 4287 (1993).
[101] F. Willaime, A. Satta, M. Nastar, and O. Le Bacq, Int. J. Quant. Chem. **77**, 927 (2000).
[102] P. Söderlind, L. H. Yang, J. A. Moriarty, and J. M. Wills, Phys. Rev. B **61**, 2579 (2000).
[103] M. J. Mehl and D. A. Papaconstantopoulos, Phys. Rev. B **54**, 4519 (1996).
[104] A. P. Sutton, M. W. Finnis, D. G. Pettifor, and Y. Ohta, J. Phys. C **21**, 35 (1988).
[105] M. W. Finnis, *Interatomic forces in condensed matter* (Oxford University Press, 2003).
[106] D. G. Pettifor, private communication.
[107] D. Nguyen-Manh, A. P. Horsfield, and S. L. Dudarev, Phys. Rev. B **73**, 020101(R) (2006).
[108] P. Derlet, D. Nguyen-Manh, and S. L. Dudarev, submitted to Phys. Rev. B.
[109] A. A. Griffith, Philos. Trans. R. Soc. London A **221**, 163 (1921).
[110] L. Vitos, A. V. Ruban, J. Kollar, and H. L. Skriver, Surf. Sci. **411**, 186 (1998).
[111] H. L. Meyerheim, D. Sander, R. Popescu, P. Steadman, S. Ferrer, and J. Kirschner, Surf. Sci. **475**, 103 (2001).
[112] J. S. Luo and B. Legrand, Phys. Rev. B **38**, 1728 (1988).
[113] R. Yu, H. Krakauer, and D. Singh, Phys. Rev. B **45**, 8671 (1992).
[114] J. G. Che, C. T. Chan, W.-E. Jian, and T. C. Leung, Phys. Rev. B **57**, 1875 (1998).
[115] J. Feydt, A. Elbe, H. Engelhard, G. Meister, C. Jung, and A. Goldmann, Phys. Rev. B **58**, 14007 (1998).
[116] J. F. Peck and D. A. Thomas, Trans. TMS-AIME **221**, 1240 (1961).
[117] P. F. Browning, C. L. Briant, K. Rajan, and B. A. Knudsen, Eng. Failure Anal. **2**, 105 (1995).
[118] M. Mrovec, T. Ochs, C. Elsässer, V. Vitek, D. Nguyen-Manh, and D. Pettifor, Z. Metallkd. **94**, 244 (2003).
[119] V. Vitek, Scripta Metallurgica **4**, 725 (1970).
[120] P. D. Bristowe and A. G. Crocker, Phil. Mag. **31**, 503 (1975).
[121] M. Mrovec, Y. Cheng, C. Elsässer, and P. Gumbsch, in *Proc. Multiscale Materials Modeling*, edited by P. Gumbsch (Faunhofer IRB Verlag, 2006), p. 213.
[122] W. Sigle, Phil. Mag. A **79**, 1009 (1999).
[123] B. G. Mendis, Y. Mishin, C. S. Hartley, and K. J. Hemker, Phil. Mag. A **86**, 4607 (2006).
[124] M. S. Duesbery, V. Vitek, and J. Cserti, in *Understanding Materials: Professor Sir Peter Hirsch Festschrift*, edited by C. J. Humphreys (The Institute of Materials, London, 2002), p. 165.
[125] W. Xu and J. A. Moriarty, Phys. Rev. B **54**, 6941 (1996).
[126] W. Xu and J. A. Moriarty, Comp. Mater. Sci. **9**, 348 (1998).
[127] S. Ismail-Beigi and T. A. Arias, Phys. Rev. Lett. **84**, 1499 (2000).
[128] Y. Juan and E. Kaxiras, Phil. Mag. A **74**, 1367 (1996).
[129] O. N. Mryasov, Y. N. Gornostyrev, and A. J. Freeman, Phys. Rev. B **58**, 11927 (1998).
[130] R. Mikulla, G. Schaaf, and H. Trebin, Phil. Mag. Lett. **79**, 721 (1999).
[131] S. L. Frederiksen and K. W. Jacobsen, Phil. Mag. **83**, 365 (2003).
[132] J.-A. Yan, C.-Y. Wang, and S.-Y. Wang, Phys. Rev. B **70**, 174105 (pages 5) (2004).
[133] H. VanSwygenhoven, P. M. Derlet, and A. G. Froseth, Nat. Mater. **3**, 399 (2004).
[134] C. Shen and Y. Wang, Acta Mater. **52**, 683 (2004).
[135] K. J. Bowman and R. Gibala, Acta Metal. Mater. **40**, 193 (1992).
[136] N. A. Stelmashenko, M. G. Walls, L. M. Brown, and Y. V. Milman, Acta Metal. Mater. **41**, 2855 (1993).
[137] X. Qiu, Y. Huang, W. D. Nix, K. C. Hwang, and H. Gao, Acta Mater. **49**, 3949 (2001).